

Active particle in a very thin interfacial droplet

Airi N. Kato¹, Kaili Xie^{1,2}, Benjamin Gorin¹, Jean-Michel Rampnoux¹, and Hamid Kellay^{1*}

¹ *Laboratoire Ondes et Matière d'Aquitaine, Université de Bordeaux, Talence 33405, France and*

² *Van der Waals-Zeeman Institute, Institute of Physics, University of Amsterdam, 1098XH Amsterdam, The Netherlands*

(Dated: January 17, 2025)

A single light-driven Janus particle confined in a very thin oil droplet at an air–water interface displays intriguing dynamics. While laser activation induces rapid horizontal motion (1 mm s^{-1} – 1 cm s^{-1}) by thermal Marangoni flow, the particle exhibits unexpected periodic circular motions or intermittent irregular motions. We show that the periodic trajectories are the result of a coupling between the self-propulsion of the particle and the spatiotemporal droplet thickness changes. We propose a simple model where the properties of the active particle trajectories are governed by capillary forces and torques due to the confinement of the particle in the thin droplet.

Soft boundaries, such as droplets [1–6], vesicles [7–9], and flexible membranes [10, 11] can serve as soft confinements that active particles can deform and reshape. These boundaries, in turn, influence particle dynamics. Droplet systems are particularly intriguing because the interface can trap or alter particle dynamics [12–17] but can also induce Marangoni flows driven by concentration [18–23] or temperature gradients [24, 25], offering a significantly more efficient and faster propulsion mechanism compared to self-diffusiophoresis.

Most studies to date have focused on the behavior of active particles confined in three-dimensional droplets, where low interfacial tension can lead to deformation by local mechanical pressure [2], or where the active particles maintain shape stability through activity [3]. However, the physical mechanisms underlying the interplay between activity and interfacial effects remain poorly understood. Thin films, thin droplets on substrates [26], and interfaces [27, 28] provide simplified yet representative systems to explore these questions. Such geometries could help clarify the roles of interfacial tension, active forces, and strong confinement in shaping particle behavior.

In this Letter, we study the dynamic behaviors of a light-driven Janus particle (JP) strongly confined in a very thin, lens-like oil droplet at an air–water interface. Our main observation is that Marangoni-driven fast JP motions exhibit diverse temporal features depending strongly on the droplet geometry confining the particle. We show that the underlying mechanisms governing the particle trajectories arise from the dynamic coupling between the JP motions and the droplet thickness profile, clarifying the role of capillary confinement in setting active particle trajectories and motions.

Self-propelled Janus particles (JPs), made of polystyrene spheres, of radius $a = 5\text{ }\mu\text{m}$, with a half-coated metal layer (see details in Supplementary Material [29]) were prepared and suspended in tetradecane oil. The suspension was then placed onto an aqueous subphase (ultrapure water with 6.8 mM NaCl) in a Petri dish and chopped with a needle to

create separated droplets with radii $R = 10$ – $600\text{ }\mu\text{m}$, as illustrated in Fig. 1(a). We here focus primarily on the dynamics of a single JP within a droplet to avoid the complexity of multiple JPs such as aggregation in the thin droplet due to the long-range capillary bridge attraction [30]. The activity of JPs can be tuned by the illumination intensity I of a top-hat profile laser (wavelength: 532 nm and radius: 108 μm) [3]. Initially, the center of the illumination area was aligned with the center of the stationary droplet. The dynamics of the JP and the droplet were visualized using an inverted microscope (Axio Observer, Zeiss) equipped with a camera (Orca Flash 4.0 from Hamamatsu or Phantom v640 from Vision Research Inc.).

The static droplet thickness profiles $h(r)$ were reconstructed from the interference fringe pattern of the droplet, as shown in Fig. 1(b) and Appendix A. The profile can be fitted by

$$u(r) = -u_0 \ln \frac{r}{R} + u_2 \frac{R^2 - r^2}{2R^2}. \quad (1)$$

Here r is the distance from the center of the drop, u_0 is a constant and $u_2 = p_0 R^2 / \gamma$, where p_0 and γ are the constant internal pressure and the interfacial tension. Here we assumed the symmetry of the oil droplet with $\theta_1 = \theta_2$, the profile simplifies to $u(r) = h(r)/2$. As defined in Fig. 1(c), u_0 , u_2 , R can be determined from the droplet volume V [29], the three-phase contact angles θ_C , and the wetting angle θ_W . The angles θ_C and θ_W are estimated using the profiles in Fig. 1(b) as $\theta_C \simeq 0.58^\circ \pm 0.30^\circ$ and $\theta_W \simeq 23.52^\circ \pm 7.12^\circ$, where the ranges are the standard deviations. (see Fig. S1 [29] for the probability distributions). Thus, the droplet is extremely thin and has a steep profile at the periphery of the JP as in the schematics of Fig. 1(a) and (c).

We now turn to explore how the thin droplets regulate the self-propelled JP motion in confinement. We observe various planar JP fast motions with distinct temporal features using droplets with different sizes under different laser illumination intensities. Within the droplet,

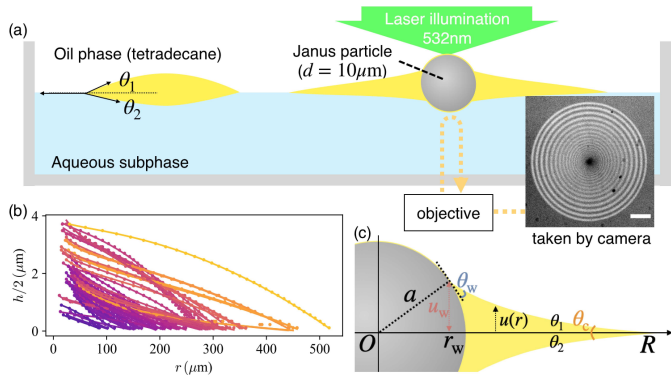


FIG. 1. Experimental setup and thin oil droplet profiles with a Janus particle. (a) Schematics of the interfacial droplets with and without a JP. The inserted image is an example of a droplet with a JP (the black dot in the center). Scale bar=100 μm . (b) Interfacial profiles $u(r) = h(r)/2$ of droplets with a static JP. The dots correspond to the measured ($r_m, h_m/2$) values using the fringes, and the solid lines are the fits to Eq. (1). The colors are set by R . (c) Schematic of the lens-like geometry.

the JP can undergo either regular motions (circular, ellipsoidal, and occasionally back-and-forth motion) with clear periodicity or irregular motions with intermittency (see Fig. 2 and Supplementary videos S1 and S2 [29]). In the regular regime, the JP can maintain a periodic motion with a typical velocity of 1 cm s^{-1} for more than 17 s (within the limit of our observation time). In contrast, in the irregular regime, the motion of the JP is intermittent, and the trajectory becomes rather chaotic.

To comprehend the variety of JP motions, we first characterize the JP dynamics in steady states by using the time series of the velocity and examining the power spectral density (PSD): $S_{vv}(f) := |\hat{v}_x(f)|^2 + |\hat{v}_y(f)|^2$, where $\hat{v}_j(f) := \frac{1}{N} \sum_{k=0}^{N-1} v_j(t_k) e^{-2\pi i f t_k}$ ($j = x, y$). Here t_k is the time and N is the total number of measurements. Note that we here focus on the steady-state behaviors of JPs within droplets with a roughly constant radius during the entire trajectory. The power spectra of the velocity time series of different trajectories show a prominent peak at a fundamental frequency f_p with a relative amplitude $a_p := S_{vv}(f_p)/S_{vv}(0)$ as shown in Fig. 3(a), satisfying $a_p \sim f_p^2$ (see details in [29]). However, two types of spectra can be distinguished: regular trajectories generally give rise to spectra with well-defined sharp peaks with large amplitudes, while irregular motions give rise to broad spectra with smaller amplitudes. We find a relationship $v_{\text{rms}} \approx \bar{r} \cdot (2\pi f_p)$, which is valid for both regular and irregular motions across all our observations. Here, $v_{\text{rms}} := \sqrt{|\mathbf{v}(t)|^2}$ represents the time-averaged speed during steady states, while \bar{r} represents the mean radius of the trajectory. Each JP-droplet combination has different values of I, R, θ_C , and θ_W , raising the question of which parameters are essential in determining whether

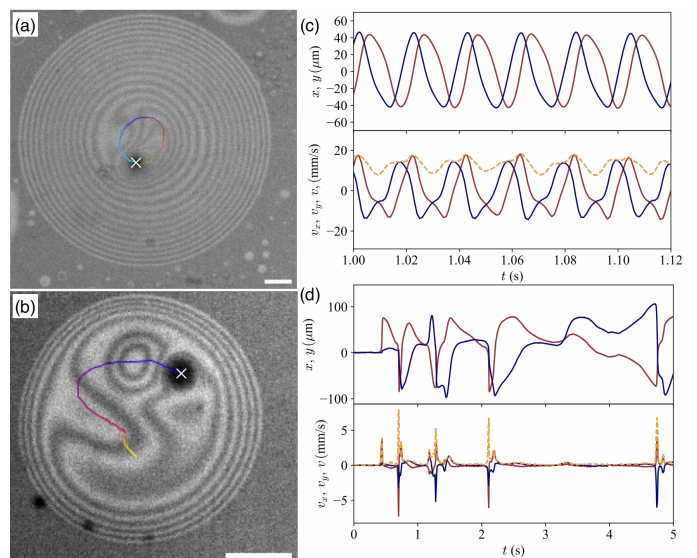


FIG. 2. Examples of regular and irregular motions of JPs. (a, b) Snapshots of a regular (a) and irregular (b) motion in a droplet under activation corresponding to $t = 0.72 \text{ s}$ and $t = 1.03 \text{ s}$ of (c) and (d) under illumination $I = 426 \text{ W/cm}^2$ (a) and $I = 415 \text{ W/cm}^2$ (b). The droplets have radii $R = 239.08 \mu\text{m}$ and $158.13 \mu\text{m}$, respectively. The trajectories drawn are for a duration of 20 ms (a) and 0.73 s (b) and are directed from yellow to blue. The JP positions are marked by “x.” See also Supplemental videos 1 and 2 [29]. (c, d) Positions $x(t), y(t)$, velocities $v_x(t), v_y(t)$, in the plane of the interface, corresponding to (a, b). The red and blue lines are for x, y -components, and the orange dashed lines indicate total speeds $v(t)$.

the JP motion is regular or irregular. Here, we further find a correlation between the frequency f_p and the contact angle θ_C as shown in Fig. 3(c).

Similarly to light-driven JPs at a planar single interface [24, 25], we believe that our JPs are driven by a thermal Marangoni flow at speed $v_p \sim -d\gamma/dT \cdot \frac{\Delta T}{\eta_o}$, where T is the temperature and η_o the viscosity of the liquid. This results in velocities of $\mathcal{O}(1 \text{ cm s}^{-1})$ for the air-oil interface and $\Delta T \sim 1 \text{ K}$, moving with its metal side facing forward due to the reaction to the Marangoni flows which go from the hot to the cold region.

To support this, we conducted similar experiments by replacing a JP with a gold core-shell particle [29]. Heating by laser illumination changed the fringes symmetrically, which resulted in no significant motion. We thus believe, the polarity of the JP is essential, unlike the case of reference [31]. In addition, the JP generated flow only locally, as suggested by additional experiments using tracer particles (see Sec. XIV [29] and Supplemental Video 3).

Previous studies on thermal Marangoni surfers at an interface showed that the particles propelled at constant speed $v_p \propto \Delta T/\eta_o \propto I$ both at planar [24, 25] and curved interfaces [32, 33]. In contrast, the speed of our JPs

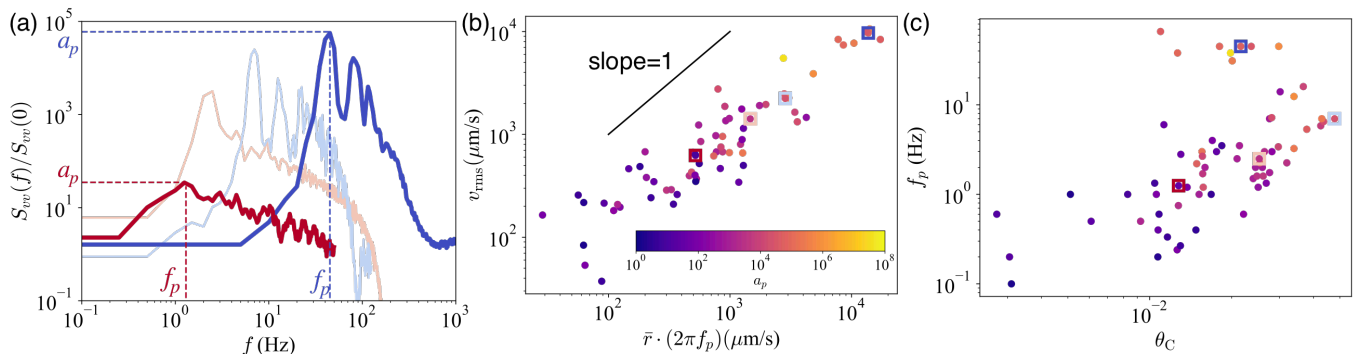


FIG. 3. Analysis of various trajectories in steady states. (a) Typical examples of PSDs. Regular (blue): $I = 426 \text{ W/cm}^2$ corresponding to Fig. 2 (a,c); irregular (red): $I = 415 \text{ W/cm}^2$ corresponding to Fig. 2 (b,d). The other two curves represent intermediate cases in terms of the peak heights ($I = 565 \text{ W/cm}^2$, 511 W/cm^2). The characteristic frequencies f_p and corresponding amplitudes a_p of the main peaks of the spectra are indicated by dashed lines. (b) Relationship between the RMS velocity v_{rms} and $\bar{v} \cdot (2\pi f_p)$. (c) Correlation between the frequency f_p and the contact angle θ_C . In (b, c), the corresponding cases of (a) are marked by the square of the same colors.

changes in time through the coupling of the JP motion and the interfacial profile, as seen through the changes of the fringe pattern in Fig. 2(a, b). Notably, the coupling occurs due to the thin nature of the oil droplets, as demonstrated in our thin film experiments where $v_p \propto I$ is valid only for a thick film $h \approx 12a$, not in a thin film $h \approx 2a$ (see Sec. VIII of [29]).

The coupling of the motion of the particle to the thickness profile changes is very complex when heating is present due to fluid flow including thermal Marangoni flow and the presence of forces exerted on the JP and due to the time-dependent inhomogeneous thickness profile. This force can be understood as a type of capillary force acting on the particle [34, 35] when it is embedded in a thin film with thickness gradients present. The local capillary force proposed in reference [35] is rewritten in its two-dimensional version:

$$\mathbf{F}(\mathbf{r}) = -\frac{\pi\gamma(h(\mathbf{r}) - h_e)}{1 + \left(\frac{\partial h}{\partial \mathbf{r}}\right)^2} \nabla h, \quad (2)$$

where h_e is the equilibrium wetting thickness for the particle.

We utilize Eq. (2) and estimate the force using the reconstructed droplet thickness profile during the steady circular motion. A snapshot of such a profile is shown in Fig. 4(a). The inhomogeneous profile around the JP results in a non-zero net force \mathbf{F}^{cap} and torque T^{cap} exerted on the JP as defined in the inset of Fig. 4(a). For the estimation method, see Appendix B. We obtained $\mathbf{F}^{cap} = (F_r^{cap}, F_\theta^{cap}) \approx (-3 \cdot 10^1 \text{ nN}, 1 \cdot 10^1 \text{ nN})$ and $T^{cap} \approx 3 \cdot 10^{-16} \text{ N m}$, and the values remain similar in other snapshots of the dynamics, including their signs. Note that the capillary force field is not conservative and thus the torque T^{cap} is nonzero. This is partially because the capillary force (Eq. (2)) is nonlinear. In addition, the equilibrium thickness h_e in Eq. (2) should not be constant

but varies spatiotemporally due to the fluid flow and the asymmetric heating, etc.

The JP feels a centripetal force of $\mathcal{O}(10 \text{ nN})$ and given by F_r^{cap} , which is comparable to the viscous force (in bulk) $F_v = 6\pi a \eta_o v_p \sim 1 \text{ nN} - 10 \text{ nN}$ for $v_p \sim 1 \text{ mm s}^{-1} - 10 \text{ mm s}^{-1}$. The positive azimuthal force $F_\theta^{cap} > 0$ means the JP is pushed forward. We often see a thinning at the tail of the JP, as seen also in Fig. 2(a,b), so the rear profile becomes steeper, which pushes the JP forward. The positive torque $T^{cap} > 0$ for the counterclockwise circular motion means an inward rotation of the JP polarity. The estimated value of the torque is comparable to the viscous torque $T^{vis} = \xi_r \Omega \sim 4 \cdot 10^{-16} \text{ N m}$ where $\xi_r = 8\pi a^3 \eta_o$, for $\Omega = 45 \text{ Hz}$ rotation assuming the JP is rotating at the same frequency as that of the circular motion. Therefore, the circular motion can be understood by the combination of the capillary centripetal force and the capillary positive torque, as well as a self-propulsion.

Here, to better understand the mechanism of the steady circular motion more quantitatively, we consider the following model with an overdamped equation of motion and rotation by capillarity:

$$0 = -\xi(\dot{\mathbf{r}} - v_p \hat{\mathbf{p}}) - k\mathbf{r} \quad (3)$$

$$0 = \mathbf{T}^{cap} - \xi_r \Omega \quad (4)$$

$$\frac{d\hat{\mathbf{p}}}{dt} = \Omega \times \hat{\mathbf{p}}, \quad (5)$$

where Ω and $\hat{\mathbf{p}}$ are the angular velocity of the JP self-rotation and the JP polarity. The particle is powered by the self-propulsion force $F_{\text{sp}} := \xi v_p$, whose value can be shifted by nonzero F_θ^{cap} though. The particle also feels the viscous damping and the capillary force in the direction \mathbf{r} or centripetal force which is approximated, for simplicity and ease, as $-k\mathbf{r}$ with k given by

$$k = 4\pi\gamma \tan^2 \theta_C, \quad (6)$$

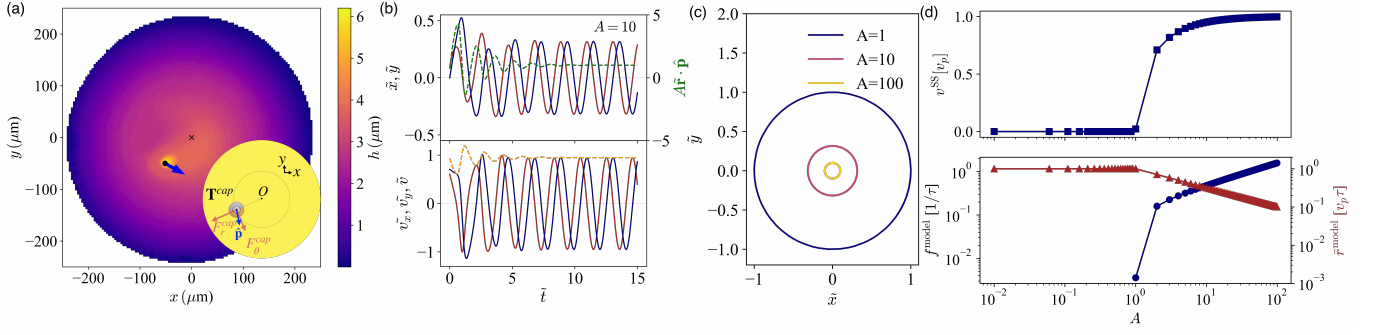


FIG. 4. Capillarity-induced circular motion. (a) Reconstructed thickness profile of a snapshot of the drop with the particle undergoing circular motion ($f_p \approx 45\text{Hz}$, $I = 565\text{ W/cm}^2$). The black dot and the arrow indicate the particle position and the propelling direction. The center of the droplet is marked as \times . Inset: Schematic for the capillary force and torque exerted on the JP in a thin droplet as well as the orientation $\hat{\mathbf{p}}$. (b) Examples of the time evolution of position $\tilde{x}(t)$, $\tilde{y}(t)$ and torque $A\tilde{\mathbf{r}} \cdot \hat{\mathbf{p}}$ (red, blue and green in the top figure). The corresponding $\tilde{v}_x(t)$, $\tilde{v}_y(t)$, and speed $\tilde{v}(t)$ (orange) are in the bottom figure. For this case, $A = 10$, $\mathbf{r}|_{t=0} = (0.1, 0)$, and $\hat{\mathbf{p}}|_{t=0} = (1/\sqrt{2}, 1/\sqrt{2})$ are used. (c) The limit cycles for different parameters. (d) Steady-state values of the speed v^{SS} , frequency f^{model} and the radial length \tilde{r}^{model} for each parameter A .

derived via the excess interfacial energy by the lowest order deformation of the droplet profile (see the derivation [29]). This expression matches with Eq. (2) in the limit where the profile is considered locally linear. The centripetal force $|k\tilde{r}| \sim \mathcal{O}(10\text{ nN})$ using the measured θ_C is consistent with the estimation from the profile (F_r^{cap}). Experimentally, the capillarity-induced centripetal force can be determined via the relaxation dynamics soon after switching off the laser illumination (see Sec. VII [29]). Neglecting inertia and the azimuthal motion, this force balances the viscous friction allowing to obtain direct estimates of the value of the spring constant k .

The capillary torque \mathbf{T}^{cap} rotates the particle, and the polarity rotates accordingly. Here we may assume that the capillary torque satisfies $\mathbf{T}^{\text{cap}} = \Gamma(\mathbf{r} \times \hat{\mathbf{p}})$ with the coefficient $\Gamma > 0$ for the observed positive torque. It can be natural to assume the magnitude of the capillary torque to be proportional to that of the capillary force and zero torque for a strictly radial $\hat{\mathbf{p}}$. The Eqs. (3-5) are summarized as the following nonlinear equations non-dimensionalized by $\tilde{t} := \tau t$, $\tilde{\mathbf{r}} := \mathbf{r}/v_p\tau$, $A := \frac{v_p\tau^2\Gamma}{\xi_r}$, with $\tau = \xi/k$, read

$$\frac{d\hat{\mathbf{p}}}{d\tilde{t}} = A \{(\tilde{\mathbf{r}} \cdot \hat{\mathbf{p}})\hat{\mathbf{p}} - \tilde{\mathbf{r}}\} \quad (7)$$

$$\frac{d\tilde{\mathbf{r}}}{d\tilde{t}} = \hat{\mathbf{p}} - \tilde{\mathbf{r}}. \quad (8)$$

The equations (7) and (8) were numerically solved using a Python code, and the results are shown in Fig. 4(c,d). Unless the initial polarity is strictly radial, the dynamics results in steady states with either periodic circular motions at a frequency f^{model} with constant torque and speed for $A \geq 1$, or in static states without any motion for $A < 1$. In fact, the static states were observed experimentally for a small laser illumination (see Fig. S2 [29]). The steady circular trajectories, namely, the limit cycles,

are shown in Fig. 4(c). Large torques, fast propulsion velocities v_p , or large values of τ all result in large values of A , leading to rotation with a smaller radius \tilde{r} . The steady-state speed $v^{\text{SS}} := \tilde{r}^{\text{model}} \cdot (2\pi f^{\text{model}})$ for periodic motions, (set to zero for static states) is shown in Fig. 4(d). The speed comparable to v_p is consistent with our experimental observations. In addition, the numerical solution leads to the relationships $f^{\text{model}} \propto \sqrt{\frac{v_p\Gamma}{\xi_r}}$ and $\tilde{r}^{\text{model}} \propto \sqrt{\frac{v_p\xi_r}{\Gamma}}$. Therefore, a larger capillary torque Γ results in motions at a higher frequency f^{model} . Considering the experimental observation that a larger θ_C leads to higher-frequency motion (f_p) as shown in Fig. 3(c), Γ must increase with θ_C . Since $f^{\text{model}} \sim \mathcal{O}(10\text{Hz}-100\text{Hz})$ for $\tau \sim 10^{-2}\text{s}$ (for the regular cases), the frequency range is also consistent with our measurements.

Note that the back-and-forth motions, irregular motions, and transient behaviors are beyond our model. Still, the back-and-forth motion might be understood as a transient state to a circular motion or a result of out-of-plane rotation (see discussion in Sec. VIII [29]). Irregular motions—should be much more complex—accompany the transient thickness changes close to the JP (see discussion in Sec. VII [29] and Supplemental Video 4 [29]), which may cause the time-dependent capillarity. Moreover, it is worth noting that, in a transient case with an apparent planar dilation (increase in R), periodic circular motion turned to irregular motion suddenly (see Supplemental Video 5 [29]). This suggests that the decrease in θ_C due to the dilation and the oil volume conservation may have driven the system into an irregular state as the droplet became much thinner.

In conclusion, we observed novel dynamics of active Janus particles confined in thin interfacial droplets. The coupling between droplet thickness and particle motion induces circular motion and other non-trivial trajec-

ries due to the strong confining geometry. We proposed a simple model where capillarity plays a major role in explaining the major observations of this study. Insights from studying active particles in thin films could provide a crucial understanding for developing novel active counterparts of particle-based soft matter systems, such as suspension films, capillary suspensions, and Pickering emulsions. The interplay between interfacial properties and activity is expected to yield unique characteristics in activity-controlled functional materials, where manipulating activity offers new avenues for creating smart and responsive systems.

We acknowledge the support of the French Agence Nationale de la Recherche (ANR), under grant N° ANR-22-CE06-0007-02. We thank T. Bickel, Y. Tagawa, K. A. Takeuchi for helpful and interesting discussions. We are particularly indebted to A. Würger for numerous discussions and for his calculation of the drop profile as well as the centripetal force.

* hamid.kellay@u-bordeaux.fr

- [1] T. Sanchez, D. T. N. Chen, S. J. DeCamp, M. Heymann, and Z. Dogic, *Nature* **491**, 431–434 (2012).
- [2] R. Adkins, I. Kolvin, Z. You, S. Witthaus, M. C. Marchetti, and Z. Dogic, *Science* **377**, 768 (2022).
- [3] K. Xie, B. Gorin, R. T. Cerbus, L. Alvarez, J.-M. Rampnoux, and H. Kellay, *Physical Review Letters* **129**, 138001 (2022).
- [4] G. Kokot, H. A. Faizi, G. E. Pradillo, A. Snezhko, and P. M. Vlahovska, *Communications Physics* **5** (2022).
- [5] R. Sakamoto, Z. Izri, Y. Shimamoto, M. Miyazaki, and Y. T. Maeda, *Proceedings of the National Academy of Sciences* **119** (2022).
- [6] H. Sakuta, N. Nakatani, T. Torisawa, Y. Sumino, K. Tsumoto, K. Oiwa, and K. Yoshikawa, *Communications Chemistry* **6** (2023).
- [7] L. Le Nagard, A. T. Brown, A. Dawson, V. A. Martinez, W. C. Poon, and M. Staykova, *Proceedings of the National Academy of Sciences* **119**, e2206096119 (2022).
- [8] H. R. Vutukuri, M. Hoore, C. Abaurrea-Velasco, L. Van Buren, A. Dutto, T. Auth, D. A. Fedosov, G. Gompper, and J. Vermant, *Nature* **586**, 52 (2020).
- [9] S. C. Takatori and A. Sahu, *Physical Review Letters* **124**, 158102 (2020).
- [10] A. Deblais, T. Barois, T. Guerin, P. Delville, R. Vaudaine, J. Lintuvuori, J. Boudet, J. Baret, and H. Kellay, *Physical Review Letters* **120**, 188002 (2018), publisher: American Physical Society.
- [11] G. Junot, G. Briand, R. Ledesma-Alonso, and O. Dauchot, *Physical Review Letters* **119**, 028002 (2017), publisher: American Physical Society.
- [12] X. Wang, M. In, C. Blanc, M. Nobili, and A. Stocco, *Soft Matter* **11**, 7376 (2015).
- [13] J. Deng, M. Molaei, N. G. Chisholm, and K. J. Stebe, *Langmuir* **36**, 6888 (2020).
- [14] H. Gidituri, Z. Shen, A. Würger, and J. S. Lintuvuori, *Physical Review Fluids* **7** (2022).
- [15] C. Feng, J. J. Molina, M. S. Turner, and R. Yamamoto, *Physical Review Research* **4** (2022).
- [16] J. Deng, M. Molaei, N. G. Chisholm, T. Yao, A. Read, and K. J. Stebe, *Current Opinion in Colloid & Interface Science* **61**, 101629 (2022).
- [17] M. Prasad, N. Obana, S.-Z. Lin, S. Zhao, K. Sakai, C. Blanch-Mercader, J. Prost, N. Nomura, J.-F. Rupprecht, J. Fattaccioli, and A. S. Utada, *Science* **381**, 748–753 (2023).
- [18] S. Nakata, Y. Iguchi, S. Ose, M. Kuboyama, T. Ishii, and K. Yoshikawa, *Langmuir* **13**, 4454–4458 (1997).
- [19] S. Yabunaka, T. Ohta, and N. Yoshinaga, *The Journal of Chemical Physics* **136** (2012).
- [20] S. Michelin, E. Lauga, and D. Bartolo, *Physics of Fluids* **25** (2013).
- [21] Y. Koyano, N. J. Suematsu, and H. Kitahata, *Phys. Rev. E* **99**, 022211 (2019).
- [22] H. Ender, A.-K. Froin, H. Rehage, and J. Kierfeld, *The European Physical Journal E* **44**, 1 (2021).
- [23] D. Boniface, C. Cottin-Bizonne, F. Detcheverry, and C. Ybert, *Physical Review Fluids* **6**, 104006 (2021).
- [24] A. Würger, *Journal of Fluid Mechanics* **752**, 589 (2014).
- [25] K. Dietrich, N. Jaensson, I. Buttinoni, G. Volpe, and L. Isa, *Physical Review Letters* **125**, 098001 (2020).
- [26] S. Trinschek, F. Stegemerten, K. John, and U. Thiele, *Physical Review E* **101** (2020).
- [27] P. A. Ash, C. D. Bain, and H. Matsubara, *Current opinion in colloid & interface science* **17**, 196 (2012).
- [28] R. Aveyard, J. H. Clint, D. Nees, and V. Paunov, *Colloids and Surfaces A: Physicochemical and Engineering Aspects* **146**, 95 (1999).
- [29] See Supplemental Material at url for experimental and theoretical details and additional results..
- [30] C. D. Willett, M. J. Adams, S. A. Johnson, and J. P. K. Seville, *Langmuir* **16**, 9396–9405 (2000).
- [31] G. Koleski, A. Vilquin, J.-C. Loudet, T. Bickel, and B. Pouligny, *Physics of Fluids* **32** (2020).
- [32] M. Y. Ben Zion, Y. Caba, A. Modin, and P. M. Chaikin, *Nature Communications* **13**, 184 (2022).
- [33] S. C. Ganesh, J. Koplik, J. F. Morris, and C. Maldarelli, *Journal of Fluid Mechanics* **958**, A12 (2023).
- [34] J. Sur and H. Kyu Pak, *Physical Review Letters* **86**, 4326 (2001).
- [35] A. Yadav, E. J. Hinch, and M. S. Tirumkudulu, *Physical Review Letters* **122**, 098001 (2019).
- [36] B. J. Park, T. Brugarolas, and D. Lee, *Soft Matter* **7**, 6413 (2011).
- [37] K. Dietrich, D. Renggli, M. Zanini, G. Volpe, I. Buttinoni, and L. Isa, *New Journal of Physics* **19**, 065008 (2017).
- [38] K. Dietrich, G. Volpe, M. N. Sulaiman, D. Renggli, I. Buttinoni, and L. Isa, *Physical review letters* **120**, 268004 (2018).

END MATTER

Appendix A: Profile of the thin droplet.—When the relationship $|\gamma_o - \gamma_{ow}| < \gamma_w < \gamma_o + \gamma_{ow}$ holds for the interfacial tensions of γ_o (air–oil), γ_w (air–water) and γ_{ow} (oil–water), the particle-free oil droplets show a lens-like shape with small contact angles, $\theta_1 \approx 0.022$ rad

and $\theta_2 \approx 0.013$ rad derived from the Young equation for the three fluids, $\gamma_w = \gamma_o \cos \theta_1 + \gamma_{ow} \cos \theta_2$ (Fig. 1(a)). The particle-free droplets possess a quadratic profile for various radii (Fig. S1(a) [29]). In contrast, the droplet containing a JP forms a thin droplet with the JP centered, showing a circular symmetry confirmed by the fringes (see inset image of Fig. 1(a)). The radially averaged thickness profiles $h(r)$ can be reconstructed via fringe counting with the bright ring condition: $h_m = \frac{m\lambda}{2n_o}$ ($m = 1, 2, 3, \dots$, $\frac{\lambda}{2n_o} = 225\text{nm}$), where λ and n_o are the wavelength of the observation light (around 630 nm) and the refractive index of oil ($n_o = 1.43$). We assume that the most outward fringe corresponds to the phase difference 2π , and the thickness changes monotonously and continuously. The series of bright spots and corresponding thicknesses (r_m, h_m) give the thickness profile $h(r)$. From the Young–Laplace equation $\gamma \nabla^2 u(r) + p_0 = 0$, we can derive Eq. 1 which fitted well with all our measured interfacial profiles ($r_m, h_m/2$).

Since the angles θ_C are material properties determined by the Young relations, the variation may originate from metastability by agitation when creating droplets. Note

that θ_W can be understood as the apparent angle because the JP is fully covered by the oil in this study. Therefore, no contact line pinning is expected. The JP has in-plane polarity in a random direction, unlike the interfacial trapped JPs, which have a propensity to have smaller in-plane polarity depending on the surface properties [12, 25, 36–38].

Appendix B: Method to estimate capillary force and Torque from the nonequilibrium profile.—To estimate the force and torque, we assume $h_e := 2u_w$ at $r = r_w$ (see Fig. 1(c)): the estimated value of wetting thickness without laser illumination. We take a force application line cycle C_ζ with radius ζ centered at the JP. The net force and torque are calculated as $\mathbf{F}_\zeta^{cap} = \oint_{C_\zeta} \mathbf{F}(s) ds$ and $T_\zeta^{cap} = \oint_{C_\zeta} \zeta \mathbf{F}(s) \cdot \mathbf{t} ds$, where ds and \mathbf{t} are the infinitesimal length elements along the curve C_ζ and the tangential unit vector along C_ζ . Since the force field decays with ζ [29], the average within $r_w \leq \zeta \leq \zeta^{\max}$ was taken, where ζ^{\max} is a distance above which the forces and torques are negligible. Then, we can obtain the net force \mathbf{F}^{cap} and net torque T^{cap} .

Supplementary information for “Active particle in a very thin interfacial droplet”

Airi N. Kato¹, Kaili Xie^{1,2}, Benjamin Gorin¹, Jean-Michel Rampnoux¹, and Hamid Kellay^{1*}

¹ *Laboratoire Ondes et Matière d’Aquitaine, Université de Bordeaux, Talence 33405, France and*

² *Van der Waals-Zeeman Institute, Institute of Physics, University of Amsterdam, 1098XH Amsterdam, The Netherlands*

I. PREPARATION OF JANUS PARTICLES

We prepared Janus particles (JPs) by metal coating on the particle monolayer on glass substrates. Polystyrene beads (TS10, Dinoseeds) were washed by Milli-Q twice and re-suspended in Milli-Q at a volume of approximately 50%. The glass substrates are washed with soap water, rinsed by Milli-Q, and treated with a plasma cleaner for 15 minutes after drying. Particle suspension was coated using a flexible blade to make a particle monolayer on the clean glass. After drying, 10 nm chromium and 100 nm gold were subsequently deposited using an electron beam physical vapor deposition technique (EB-PVD, Meca2000). The coated particles were removed from the substrates by sonication in a water-ethanol mixture, washed with Milli-Q several times and dried at 35 degrees for a few days.

II. DROPLET THICKNESS PROFILES WITHOUT LASER ACTIVATION

Lens-shaped oil droplets can form at an air–water interface when $|\gamma_o - \gamma_{ow}| < \gamma_w < \gamma_o + \gamma_{ow}$, satisfying the Young relation for three fluids:

$$\begin{aligned}\gamma_w &= \gamma_o \cos \theta_1 + \gamma_{ow} \cos \theta_2 \\ \gamma_o \sin \theta_1 &= \gamma_{ow} \sin \theta_2,\end{aligned}\tag{S1}$$

where γ_o , γ_{ow} , γ_w are the interfacial tensions of air–oil, oil–water, and air–water interfaces. In our cases, the values shown in Table S2 hold lens-shaped oil droplet conditions, exhibiting small contact angles $\theta_1 \approx 0.022$ and $\theta_2 \approx 0.013$ by solving Eq. (S1).

Next, we discuss the profiles of oil droplets and those enclosing the immobile JP at the interface. The oil film ranges to a maximum radius of R . For the sake of simplicity, we assume the oil droplet is symmetric with $\theta_1 = \theta_2$. The interfacial profile $u(r)$ hold $u(r) = h(r)/2$, where $h(r)$ is the oil thickness. The profile $u(\mathbf{r})$ satisfies the Young–Laplace equation

$$\gamma \nabla^2 u + p_0 = 0,\tag{S2}$$

with the interface tension γ and the internal pressure p_0 in the oil phase. Putting $u_2 = p_0 R^2 / \gamma$, one readily finds

$$u(r) = -u_0 \ln \frac{r}{R} + u_2 \frac{R^2 - r^2}{2R^2}\tag{S3}$$

The three parameters u_0 , u_2 , R are determined by the droplet volume V , and the contact angles $\theta_c (= \theta_1 + \theta_2)$ and θ_w at the air–water–oil phase boundary and where the fluid interfaces meet the particle surface. For the particle-free droplet $u_0 = 0$, the second term of Eq. (S3) gives the quadratic interfacial profile. As explained in the main text, we reconstruct the thickness profile from the fringes for particle-free droplets, and droplets with a passive JP are shown in Fig. S1(a, b) with the fitting to Eq. (S3). Here we fixed R to the measured droplet radius and conducted the two-parameter fitting. The fitted parameters are shown in Fig. S1(c).

The droplet volume is readily integrated Eq. (S3):

$$V = \frac{u_0 R^2}{4} + \frac{u_2 R^2}{8},\tag{S4}$$

* hamid.kellay@u-bordeaux.fr

where we neglect terms of the order $\mathcal{O}(a^2/R^2)$, and shown in Fig. S1(d) as a function of R . The volume V is roughly proportional to R^3 , and the droplet volumes can range 1 pL–100 pL. As the volume of a JP is 0.65 pL, the volume fraction of the interfacial droplets can widely range from 0.65% to 65 %.

By the full function shape with the fitting parameters u_0, u_2 , the contact angles θ_C and wetting angles θ_W can be calculated. The probability distributions of the angles for all droplets are shown in Fig. S1(e) and (f). The three-phase contact angles θ_C slightly differ with larger variations $\theta_C \simeq 0.58^\circ \pm 0.30^\circ$ with a JP case, compared to the cases of free droplet $\theta_C \simeq 0.84^\circ \pm 0.27^\circ$. The wetting angle θ_W significantly smaller than 90 degrees suggests the sharp interfacial thickness changes around the particle.

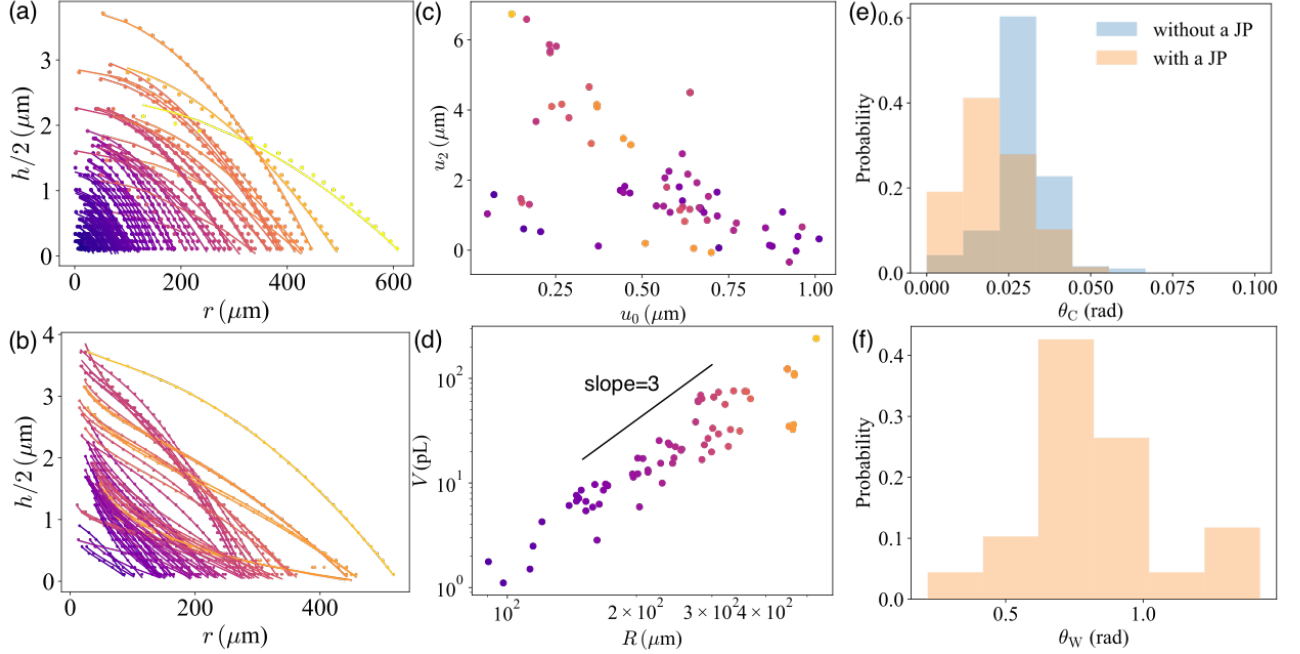


FIG. S1. (a) Interfacial profiles of particle-free droplets. Dots are from the observation of the bright rings, with fitted solid lines using the second term of Eq. (S3). (b) Interfacial profiles of droplets with a passive JP. Dots are from the observation of the bright rings, with fitted solid lines using Eq. (S3). The colors from purple to yellow of (a,b) are set by R . (c) The two fitting parameters for the fitting to (b). (d) The estimated volume V by substituting the fitting parameter u_0, u_2 to Eq. (S4) for fixed droplet radius R . (e) The probability distribution of contact angles θ_C for the free drops and the droplet with the JP. (f) The probability distribution of the wetting angle θ_W .

III. LASER BEAM FOR ACTIVATION

The detail of our setup for creating a top-hat laser beam was described in our previous paper [1]. In short, the Gaussian green laser beam (MSL532 300 mW, 532 nm wavelength) is transformed into a homogeneous top-hat profile with 108 μm radius by a beam shaper (TOPAG FBSR-20-532).

IV. DERIVATION OF THE SPRING CONSTANT OF CAPILLARY CENTRIPETAL FORCE

In the lubrication approximation, the shear stress $\sigma = \eta v/u$ (where η and u are the viscosity of the oil film and the interface height) needs to be finite, imposing zero velocity at $r = R$. Thus, one expects that the boundary of the oil droplet is rather immobile, and the moving particle takes an off-center position \mathbf{q} .

In the frame with the origin at the droplet center, the equilibrium shape is given by

$$u(\mathbf{r}) = u_0 \ln \frac{R}{|\mathbf{r} - \mathbf{q}|} + u_2 \frac{R^2 - r^2}{2R^2} - u_0 \frac{\mathbf{q} \cdot \mathbf{r}}{R^2} - u_0 \frac{2(\mathbf{q} \cdot \mathbf{r})^2 - q^2 r^2}{2R^4} + \dots, \quad (\text{S5})$$

where the additional terms assure the boundary condition $u(\mathbf{R}) = 0$. In the following, they are truncated at the quadratic order in q .

To simplify the calculation of the interfacial energy, we adopt the particle-fixed frame with coordinates $\mathbf{r}' = \mathbf{r} - \mathbf{q}$, resulting in

$$u'(\mathbf{r}') = u_0 \ln \frac{R}{r'} + u_2 \frac{R^2 - r'^2}{2R^2} + (u_0 + u_2) \frac{\mathbf{q} \cdot \mathbf{r}'}{R^2} - u_0 \frac{q^2}{2R^2} - (2u_0 + u_2) \frac{2(\mathbf{q} \cdot \mathbf{r}')^2 - q^2 r'^2}{2R^4}. \quad (\text{S6})$$

One readily verifies the boundary condition

$$u'(\mathbf{R} - \mathbf{q}) = 0, \quad (\text{S7})$$

with $\mathbf{R} = R\mathbf{e}_{r'}$.

Defining the polar angle φ through $\mathbf{r}' \cdot \mathbf{q} = r'q \cos \varphi$, and retaining the leading term in q/R only, the surface energy reads as

$$E[u'] = \frac{\gamma}{2} \int dS (\nabla u')^2 = E_0 + \frac{k}{2} q^2, \quad (\text{S8})$$

with the spring constant

$$k = 4\pi\gamma \frac{(u_0 + u_2)^2}{R^2} = 4\pi\gamma \tan^2 \theta_C. \quad (\text{S9})$$

V. SPEED AND LASER ILLUMINATION INTENSITY

The thermal Marangoni-driven JPs at the interface move at a constant speed proportional to the laser illumination intensity $v_p \propto I$ both in a planar interface [2, 3] and curved interfaces [4, 5]. As discussed in the main text, our case shows a time-dependent speed by the coupling with the capillarity. Still, we can find a correlation between the speed and the laser intensity, as shown in Fig. S2. Under a small illumination intensity, the JP remained static. Because the threshold for the motion might depend on the confined geometry of droplets, there is a coexistence region.

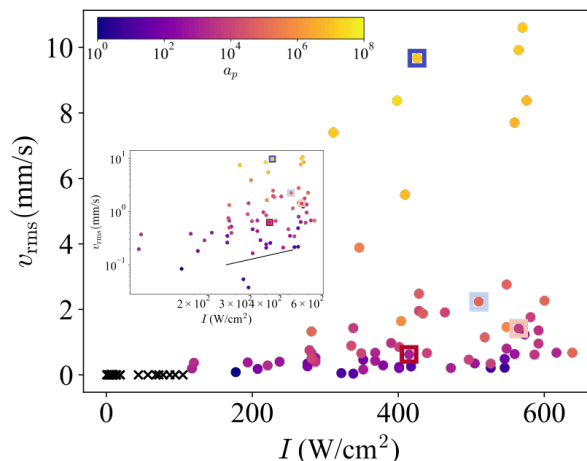


FIG. S2. (a) Laser illumination intensity and typical speed v_{rms} . No significant motion was observed for “ \times .” The red and blue squares correspond to Fig. 2 and 3(a) in the main article. Inset is in log scale with the line representing a guide to the eyes with a slope of 1. (b) Laser illumination intensity and the maximum speed. (c) Mean radial lengths \bar{r} and droplet radii R .

VI. SIGNAL PROCESSING FOR THE POWER SPECTRAL DENSITY (PSD)

To extract the peak frequency f_p in the main text, first, we smoothed the trajectory and got the velocity. To remove noise in a low-frequency region, we computed the PSDs of velocity (Fig. 3(a)) by segmenting every two seconds, windowed by a Hanning window, and then averaged.

To characterize various behaviors of JPs, we use f_p as we explained in the main text, but the relative amplitude of the spectra $a_p := S_{vv}(f)/S_{vv}(0)$ might also be used. As shown in Fig. S3, $a_p \propto f_p^2$.

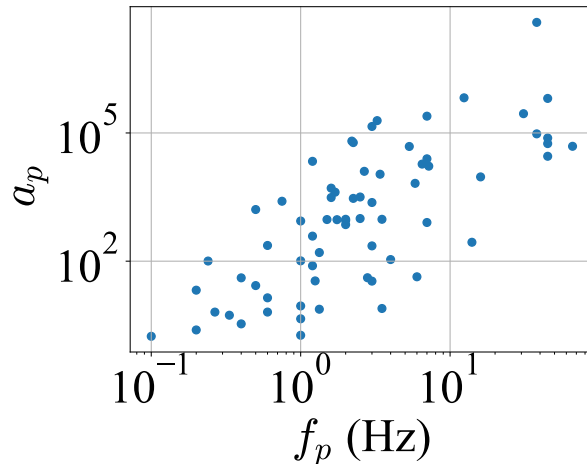


FIG. S3. Relationship between the relative amplitude of the PSD a_p and the peak frequency f_p of PSD.

VII. SUPPLEMENTAL EXPERIMENTS ON THE RELAXATION PROCESSES

To clarify the centripetal force exerted on the JP due to the interfacial profile, we conduct relaxation experiments. We observed the motion after switching off the laser at $t = t_{\text{off}}$ after activation. Experimentally, the JP relaxed to the center of the droplet, where the capillary force balances. The trajectories were not straight lines, as shown in Fig. S4(a), which can be due to the inertia and the capillary force. Figure S4(b) shows the temporal changes in radial length. They basically decay exponentially as a usual overdamped harmonic oscillator, but some trajectory shows the oscillation around the equilibrium, which means it is slightly underdamped.

The inertia is neglected in the relaxation process, then the viscous force balances with the centripetal force. Because the viscous force is proportional to v , the velocity would tell about the capillary force. Here, we neglect the azimuthal component, and the normalized force is $|v_r/v_r(t_{\text{off}})| \sim r$ as shown in Fig. S4(c), suggesting a force by a harmonic oscillator.

Therefore, assuming the overdamped harmonic oscillator

$$k\mathbf{r} + \xi\dot{\mathbf{r}} = 0, \quad (\text{S10})$$

we estimated the relaxation time $\tau = \xi/k$ from the radial speed of the relaxation process. The timescale of τ ranges from 10^{-2}s – 10^0s , as shown in Fig. S4(d). Remark that τ has little correlation with R but a correlation with the contact angle θ_C . This is understood by the spring constant depending on θ_C , as seen in Eq. (S9). A tendency exists for strong confinement (large $\tan^2\theta_C$) that showed more regular motions to result in a fast relaxation.

The relaxation time τ can be estimated via the Eqs. (S10) and (S9) assuming $\xi = 6\pi a\eta$, lead $\tau \sim 10^{-3}\text{s}$ – 10^{-2}s using physical values for oil (η_o and γ_o). The reasons for the relaxation time scale discrepancy might be due to the higher-order deformations. More regular cases have less discrepancy, which suggests the profile is closer to the lower-order deformation.

VIII. SUPPLEMENTAL EXPERIMENTS OF JANUS PARTICLES IN THIN FILM EXPERIMENTS

To see in which condition the coupling of interfacial deformation and JP motion can occur, we conducted the experiments of JPs in a thin flat film ($\sim 10\ \mu\text{m} = 2a$) and thick flat film ($\sim 60\ \mu\text{m} = 12a$), where a is the radius of JPs.

We put a known volume of the oil suspension (20 μL or 120 μL) containing JPs on distilled water in a glass Petri dish. We conducted experiments only at the center of the dish, where the effect of the meniscus is weak. We did not see the fringes without activation in the region of interest. When we began an illumination, the JP was placed

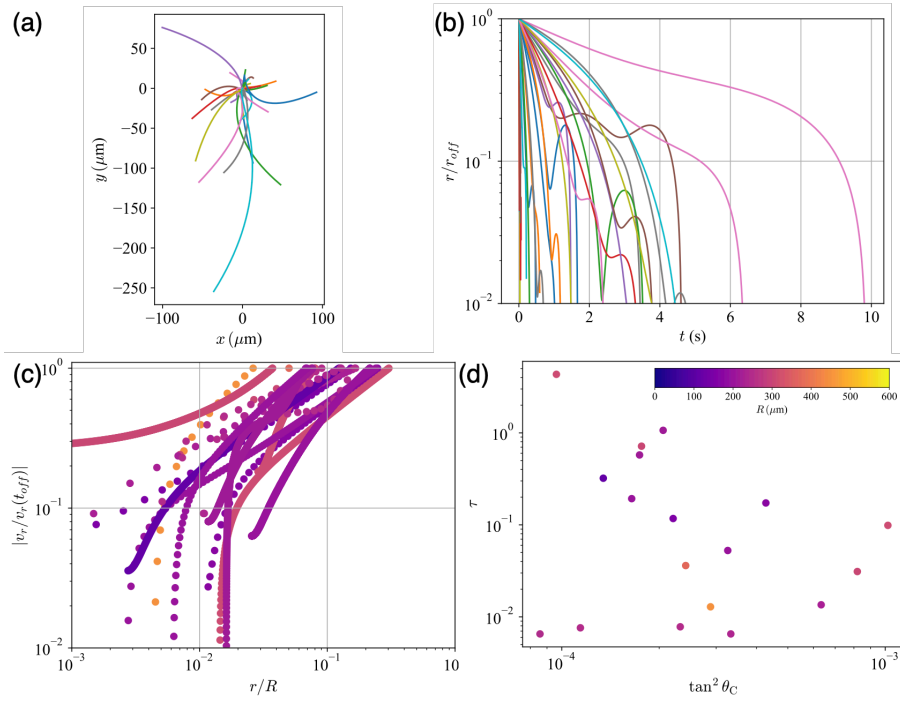


FIG. S4. Relaxation process from active state. (a) Trajectories (b) Radial position $r(t)$ normalized by the initial position. (c) Radial speed as a function of radial length r , which might suggest that the force $\propto r^\alpha$. (d) The relaxation time by an exponential fit (using the first 3/4 of the time series). (c,d) is colored by the droplet radii R .

at the illumination center, and tracked until it went out from the illuminated area. It should be noted that these experiments provide only a very short-time observation.

We measured the average speeds \bar{v} for the different laser illumination intensity I . In the thick film, the propulsion speed is almost $\bar{v} \propto I$ as shown in Fig. S5, as usual cases of Marangoni surfer powered by single interfacial flow [2–5]. Because the JP is not trapped at the interface and might stay at an arbitrary vertical position in the oil film thickness $60 \mu\text{m}$, the speed varied with samples.

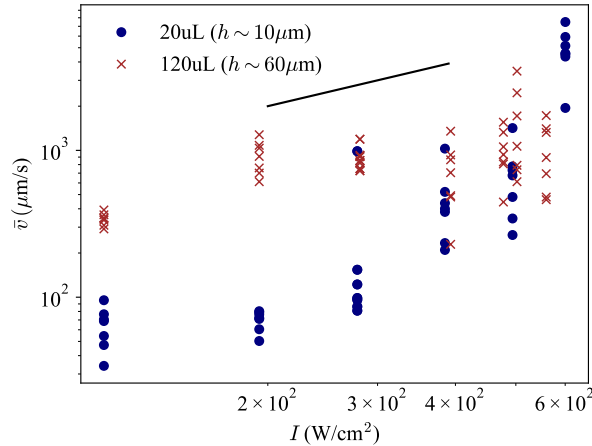


FIG. S5. Propulsion velocity \bar{v} versus laser intensity I . The solid black line with slope 1 is the guide to the eye.

In contrast, in the thin film, the propulsion speed \bar{v} is clearly different from $\bar{v} \propto I$ as shown in Fig. S5. Furthermore, we observed fringe propagation under the activation at all values of laser intensity in the ranges of $I = 109\text{--}546 \text{W/cm}^2$, while we never observed the fringe in the above thick film experiments. Unlike in a thick film, the thickness profile deforms by the activation in the thin film.

IX. METHOD TO ESTIMATE THE CAPILLARY FORCE AND TORQUE IN STEADY CIRCULAR MOTION

We take an example of periodic circular motion and estimate the capillary force and torque exerted on the JP solely from the interfacial profile. For this, we took contours from the fringes in a snapshot and assigned the height from the outer fringes. We assume that the most outward fringe corresponds to the phase difference 2π , and the thickness is continuous and monotonous. Also, we assign $h = 0$ at the edge of the droplet (three-phase contact line) and $h = 2u_w$ at the distance $r = r_w$ from the JP position. To plot, we created the grid with linear interpolation. The reconstructed thickness profiles are shown in Fig. S6(a, b). Using the expression Eq. (3) in the main text, we can obtain a force field around the JP. We took the force application circle C_ζ , and considered the net force and torque as a function of ζ , as explained in the main text. The results for the two snapshots are shown in Fig. S6(c, d) for force and (e, f) for torque, respectively. The detail function shape of $\mathbf{F}_\zeta^{cap}(\zeta)$ depends on the snapshot well, but the force and torque vanish for large ζ . This means that the interfacial deformation within a certain distance from the JP contributes to the capillary force and torque exerted on the JP. Therefore, we set the cutoff distance $\zeta_{\max} = 50 \mu\text{m}$ (The dashed lines in Fig. S6(c-f)) for averaging to avoid spurious contribution.

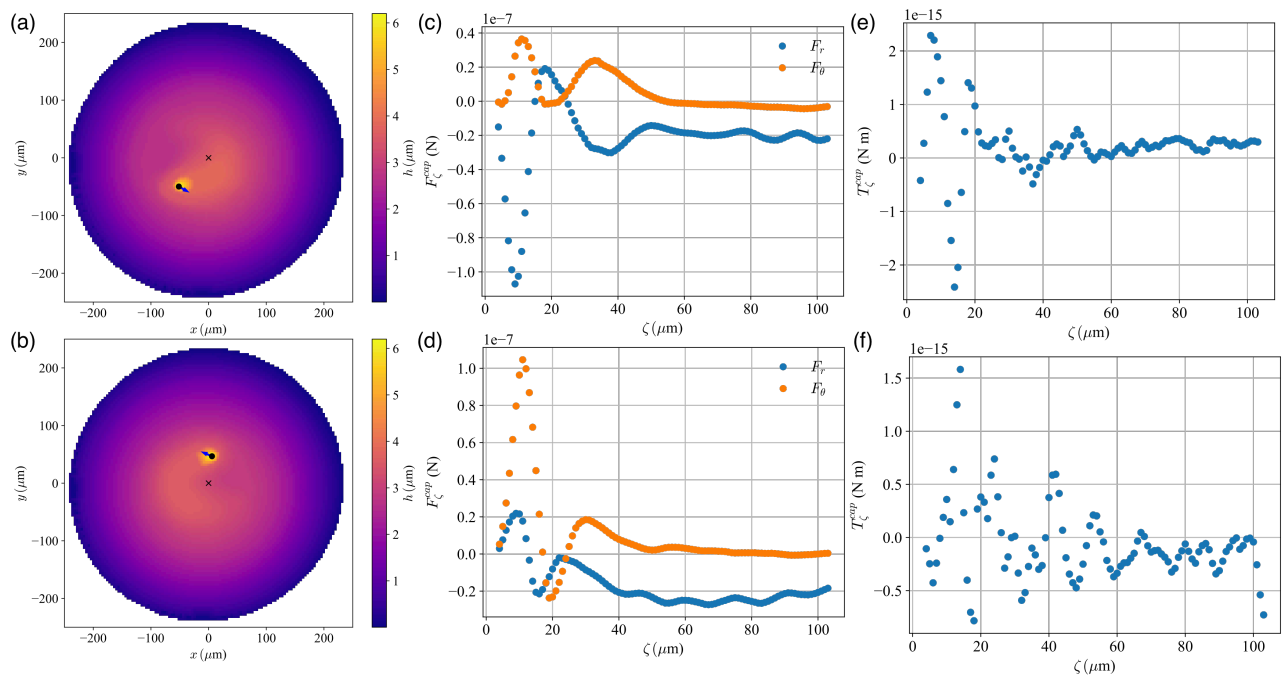


FIG. S6. (a, b) The reconstructed height profile for two different moments of the same counterclockwise circular motion. ((a) is same as Fig. 4(a) in the main paper.) (c, d) Capillary forces around the circle C_ζ for (a, b) respectively. (e, f) Capillary torque around the circle C_ζ for (a, b) respectively.

X. SUPPLEMENTAL EXPERIMENTS USING SYMMETRIC PARTICLES

To clarify the role of polarity in the motion of Janus particles, we used core-shell particles of the same size as Janus particles ($10 \mu\text{m}$), made of polystyrene spheres fully coated by gold. (SG10u, nanocs; coating thickness: 5–10nm).

For droplets with single core-shell particles, we confirmed the fringe changes by laser illumination, which is considered that heating changes the profile close to the particle (see also discussion in Sec.XI). Importantly, **no motion was driven even under high-intensity illumination over $550 \text{ W}/(\text{cm}^2)$** . Although the gold thickness is around ten times smaller than our JP's, a cluster of core-shell particles can lead to a self-rotation or a regular motion like a JP. Therefore, we believe a significant asymmetry is necessary for self-propulsion, which is different from the instability of global flow by a heated particle [6].

XI. INTERFACIAL PROFILE CHANGES BY HEATING

The interfacial profile changes can be triggered by heating of the JP, as well as a hydrodynamic flow. In this section, we discuss that a heating effect exists realistically. The temperature gradient changes both the interfacial tension spatially $\gamma(r)$ as well as the boundary condition of wetting angle θ_W which is determined by the interfacial tensions γ for the JP and all fluid (air, oil, and aqueous phase).

As shown in the following, we observed the inward fringe displacement for a symmetric heated particle in a droplet. In addition, we observed the outward propagation of fringes around a JP by a deformation of a thin flat film under a small activation. Both suggest an interfacial profile changed by heating.

We should remark that the values θ_W and $\Delta\theta_W := \theta_W(T + \Delta T) - \theta_W(T)$, as well as the detailed profile close to the JP, are not accessible so that we do not know that the interfacial profile changes are caused by wetting $\Delta\theta_W < 0$ or dewetting $\Delta\theta_W > 0$.

1. The inward fringe displacement for a symmetric heated particle in a droplet

First, we observed the inward fringe displacement for a symmetric particle in a droplet (See the Method for Sec. X). As shown in Fig. S7, the fringe close to the particle moved inward in all cases. Note that because the thickness of the gold layer is 10-time thinner compared with that of our JPs, the heating effect is not significant. Still, we observed an inward fringe displacement of around $\sim 2\ \mu\text{m}$ for the fringe nearest to the particle in our resolution.

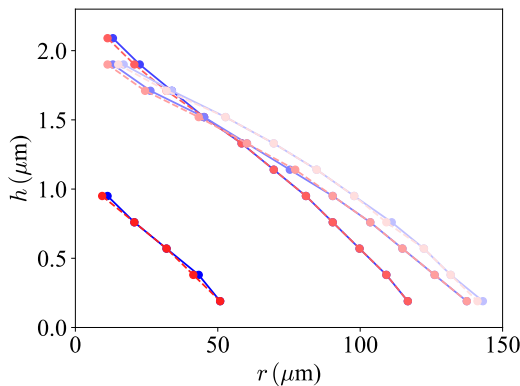


FIG. S7. Fringe symmetric displacement by heated coreshell particle. Blue: passive, Red: active (from the darker line and symbol, $I = 382, 410, 483, 614\text{W}/\text{cm}^2$). The symbols correspond to the positions of fringes. The fringes closest to the JP in our resolution moved around $2\ \mu\text{m}$.

The fringe inward displacement is an interfacial deformation, not by the changes in the refractive index. We can exclude the possibility of the refractive index changes in the following discussion.

The refractive index n usually decreases by temperature by reducing its density. For alkane, the refractive index depends on density: $n = 5 \cdot 10^{-4} \cdot \rho + 1.05$ [7], where ρ is in $[\text{kg}/\text{m}^3]$. The density ρ depends on temperature: $\rho = -0.648T_{deg} + 952.50$ around $T_{deg} = 20^\circ\text{C} - 40^\circ\text{C}$ [8]. Therefore, $n_o = -3.24 \cdot 10^{-4}T_{deg} + 1.53$. Thus, the refractive index of tetradecane n_o can be 1.428, 1.427, 1.425 at 30, 35, 40°C , which is not so large.

We observed the inward fringe motion ($\sim 2\ \mu\text{m}$) in the droplet with a coreshell particle. To judge if this is due to the interfacial shape change or the refractive index change by a temperature rise, we consider the following situation:

Let us suppose there is no shape change but only the refractive index change to $n'_o = 1.425$ at 40°C from 20°C . A certain m th fringe height changes $\Delta h_m = \frac{m\lambda}{2} \left(\frac{1}{n'_o} - \frac{1}{n_o} \right)$. Locally, such as within two fringes h and their radial length r is considered linear, so a small height difference Δh obeys $\Delta h = \frac{\lambda \Delta r}{2n_o \Delta r_0}$, where Δr_0 and Δr are the typical fringe interval and the fringe displacement. We can take $\Delta r_0 \sim 10\ \mu\text{m}$ in a large case and consider the above fringe height change Δh_m , then the m th fringe move $\Delta r \sim m \cdot (0.03\ \mu\text{m})$. In an example, $m = 11$ th fringe (the most inward fringe loop detectable) moved $2\ \mu\text{m}$, which is much larger than the value expected via refractive index change: $0.33\ \mu\text{m}$. Therefore, the fringe inward motion in the droplet with a core-shell particle is not due to the refractive index changes but a real interfacial deformation.

2. *The outward propagation of fringes around a JP in a thin flat film*

In thin film experiments in Sec. VIII, the fringes propagated from the center of the particle to the outward. The area with visible fringes increased and then started decreasing when the JP reached the edge of illumination. At a small intensity ($I = 109\text{W}/\text{cm}^2$), the fringe propagation started prior to the motion. In addition, the interfacial deformation by an active JP-powered flow due to the particle might not be symmetric. Therefore, it is plausible to consider this fringe propagation as the result of the heating effect. The fringe propagation speed was $v_{\text{fringe}} \sim 1\text{mm s}^{-1}$ at $I = 109\text{W}/\text{cm}^2$. Let us remark that this speed is much slower than the thermal capillary wave of thin films [9] ($\mathcal{O}(1\text{m s}^{-1})$), which is not our case. The interfacial profile changes by heating can explain the fringe outward motion.

XII. NON-STEADY BEHAVIOR WITH A LARGE DILATION

The importance of droplet confinement can be supported via experiments with non-steady behaviors, which were observed only for a tiny droplet under a large illumination intensity.

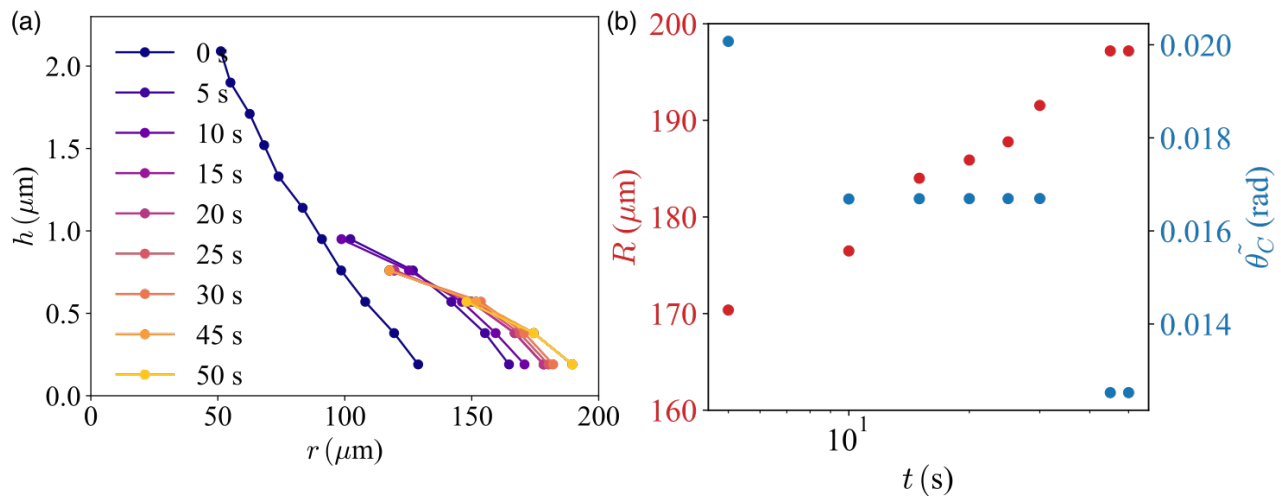


FIG. S8. Non-steady behavior under the illumination at $I = 380\text{W}/\text{cm}^2$. (a) The thickness profile changed with time. (b) Droplet radius R increases, and the contact angle decreases.

In a Supplemental Video 3 [10] and Fig. S8(a, b), the droplet radius $R(t)$ increased 46% and the approximated contact angle $\tilde{\theta}_C := \arctan(-dh/dr|_{r=R}) (\sim \theta_C)$ decrease 38% in 50 s. This dilation weakened the confinement, leading to the transition from a regular regime to an irregular one. We note that the final radius of the droplet did not change after switching off the activity. This means that the droplet goes from a metastable state to another metastable state at the same temperature. We believe a viscous dissipation drove the dilation due to the JP motion. The force per unit length for the droplet edge motion $\gamma|\cos\tilde{\theta}_C^{\text{final}} - \cos\tilde{\theta}_C^{\text{initial}}|$ is the order of 10^{-6}N m^{-1} for this large dilation case. In contrast, $\Delta T = 1\text{K}$ heating will give $|d\gamma/dT \cdot \Delta T|$, resulting in the force in the order of 10^{-4}N m^{-1} . The viscous dissipation $\sim \eta v$ gives 10^{-6}N m^{-1} for $v = 1\text{mm s}^{-1}$ whose order corresponds to the dilation's. In addition, the rise in temperature due to JP would not happen globally with the existence of the aqueous subphase working as a heat reservoir. The hypothetical temperature rise in steady state $\Delta T \rightarrow T + \Delta T$ leads to each interfacial tension change in the Young equation Eq. S1 by $\gamma = d\gamma/dT \cdot \Delta T$, but the small temperature rise such as $\Delta T = 0.6\text{K}$ lead to the bankrupt of the condition for the Young equations Eq. S1 of lens-like droplets, resulting in the formation of oil thin film in equilibrium. Therefore, droplet dilation in two-dimension was not driven by the global temperature rise but due to the motion of the active JP.

XIII. TRANSIENT TRAJECTORIES OF THE MODEL

In the model described in the main article, the particle relaxes to a limit cycle for sufficiently large A . When the initial velocity is closer to the radial direction, the effect of torque to rotate is smaller, which takes a longer time to relax to the periodic state. In that process, back-and-forth motion-like trajectories can be seen as shown in Fig. S9.

Nonetheless, an alternative scenario could involve out-of-plane rotation (Ω parallel to xy plane), which goes beyond the scope of the aforementioned model.

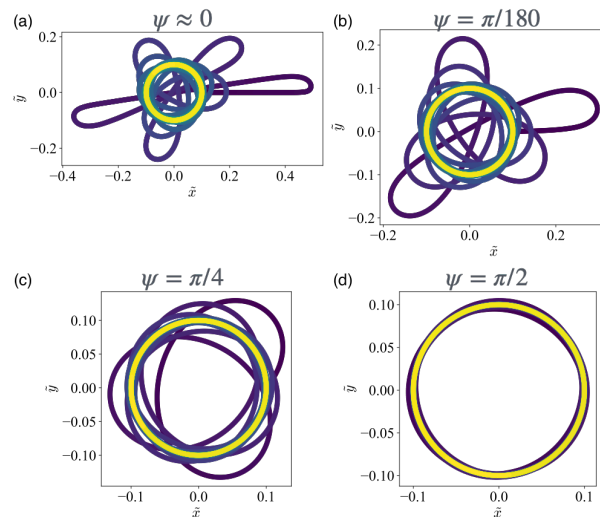


FIG. S9. The transient trajectories suggest one possible scenario for the back-and-forth motion. $A = 100$, $(\tilde{x}(0), \tilde{y}(0)) = (0.1, 0)$. Non-steady trajectories depend on how much the initial orientation $\hat{\mathbf{p}}(0) = (\cos \psi, \sin \psi)$ has an azimuthal component. The initial polarity angles ψ are changed. All trajectories go to the same limit cycle (yellow).

XIV. SUPPLEMENTAL EXPERIMENTS ADDING TRACERS

To obtain information on the fluid flow by an activation, $0.6 \mu\text{m}$ TiO_2 tracer particles were added to the oil phase. As general problems, we cannot conduct particle tracking velocimetry with enough tracers; tracers tend to stick on the surface of the Janus particle by capillary attraction, which changes the Janus particle motion itself. Thus, we put a small amount of tracer particles, and focused only on free tracers.

We observed that only tracers close to the active JP moved, which suggests the flow generated locally in the adjacent of the JP. Moreover, a tracer went to the center of a convex or concave structure (Fig. S10, as well as Supplementary Video 4.): nearly concentric fringe loops that contained no JP when the structure was vanishing. It suggests that the fringe loops mean a concave structure.

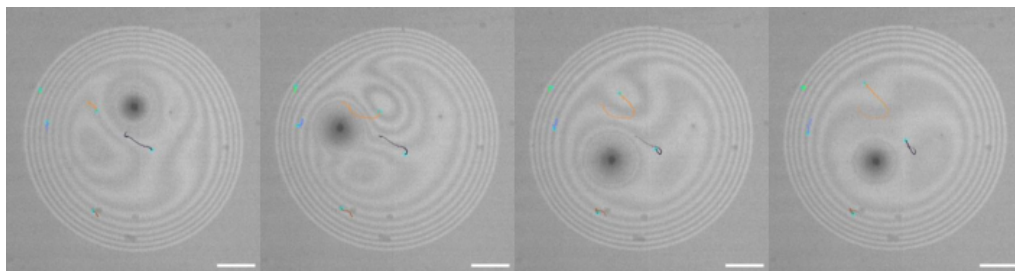


FIG. S10. Montage every 0.25 s ($I = 344 \text{ W/cm}^2$). Trajectories of some tracers are marked. The orange-marked trace went into the fringe loop that JP made at its previous position. Scalebar= $100 \mu\text{m}$

XV. LIST OF SUPPLEMENTAL VIDEOS

- S1_regular.mov Regular (periodic, circular) motion, $I = 426 \text{ W/cm}^2$.
- S2_irregular.mov Irregular motion, $I = 415 \text{ W/cm}^2$.

- **S3_largedeformation.mov** Large deformation of the droplet. Tracers (TiO_2 , $0.6 \mu\text{m}$) were in the oil phase. The acceleration of the JP led to the formation of concentric fringe loops, which did not contain the JP inside. These fringe loops are a concave structure, indicating thinning at the rear side of the JP. This modulation in thickness, which occurs away from the JP, is likely driven primarily by hydrodynamic flow. $I = 344 \text{W}/\text{cm}^2$. $\times 0.25$ play.
- **S4_escape.mov** JP escaping from the oil phase in an extremely thin case, $I = 647 \text{W}/\text{cm}^2$.
- **S5_nonsteady.mov** Non-steady case with a large dilation, $I = 380 \text{W}/\text{cm}^2$.

XVI. MATERIAL DATA

TABLE S1. Values at 20°C

	$\gamma[\text{mN}/\text{m}]$	$\rho[\text{g}/\text{mL}]$	n	$\eta[\text{mPa} \cdot \text{s}]$	$\kappa[\text{W}/(\text{m} \cdot \text{K})]$
tetradecane	26.53	0.762	1.429	2.81	0.14 (*the value of decane)
water	72.8	1	1.33	1	0.61

TABLE S2. Values related to interfaces

$\gamma_o[\text{mN}/\text{m}]$	$\gamma_w[\text{mN}/\text{m}]$	$\gamma_{ow}[\text{mN}/\text{m}]$
26.53	72.8	46.28 ^a
$d\gamma_o/dT [\text{mN}/(\text{m} \cdot \text{K})]$	$d\gamma_w/dT[\text{mN}/(\text{m} \cdot \text{K})]$	$d\gamma_{ow}/dT[\text{mN}/(\text{m} \cdot \text{K})]$
-0.144[11]	-0.151	-0.08[12]

^a calculated using the Young relation and the measured contact angles

	$\rho[\text{g}/\text{mL}]$	n	$\kappa[\text{W}/(\text{m} \cdot \text{K})]$
Polystyrene	1	1.58	1.0
Cr	7.19	-	92
Au	19.3	-	315
Our JP	1.56 (effective)	-	-

-
- [1] K. Xie, B. Gorin, R. T. Cerbus, L. Alvarez, J.-M. Rampoux, and H. Kellay, *Physical Review Letters* **129**, 138001 (2022).
[2] K. Dietrich, N. Jaensson, I. Buttinoni, G. Volpe, and L. Isa, *Physical Review Letters* **125**, 098001 (2020).
[3] A. Würger, *Journal of Fluid Mechanics* **752**, 589 (2014).
[4] M. Y. Ben Zion, Y. Caba, A. Modin, and P. M. Chaikin, *Nature Communications* **13**, 184 (2022).
[5] S. C. Ganesh, J. Koplik, J. F. Morris, and C. Maldarelli, *Journal of Fluid Mechanics* **958**, A12 (2023).
[6] G. Koleski, A. Vilquin, J.-C. Loudet, T. Bickel, and B. Pouligny, *Physics of Fluids* **32** (2020).
[7] Winoto, N. Loahardjo, K. Takamura, and N. R. Morrow, *International Oil Spill Conference Proceedings* **2014**, 1465–1473 (2014).
[8] T. V. Santos, M. F. Pereira, H. M. Avelino, F. J. Caetano, and J. M. Fareleira, *Fluid Phase Equilibria* **453**, 46–57 (2017).
[9] Y. Zhao and H. Xu, *Physical Review Fluids* **9**, L022001 (2024), publisher: American Physical Society.
[10] See Supplemental Material at url for experimental and theoretical details and additional results..
[11] A. Queimada, I. M. Marrucho, and J. Coutinho, *Fluid Phase Equilibria* **183-184**, 229 (2001).
[12] S. Zepieri, J. Rodríguez, and A. L. López De Ramos, *Journal of Chemical & Engineering Data* **46**, 1086 (2001).